Journal of Materials Chemistry C

ROYAL SOCIETY OF CHEMISTRY

PAPER

View Article Online
View Journal | View Issue

Cite this: J. Mater. Chem. C, 2026, 14, 4404

Spin-polarized carriers and ferromagnetism induced by Pt incorporation in ZnO: an experimental and DFT assessment

Subhash Sharma, *[ab] Gabriel Rojas-George,[c] C. A. Corona-García, [b] Sunil Chauhan, [d] Santosh Kumar, [e] Rajesh Kumar, [e] Javier Alonso Lopez Medina, [a] Rodrigo Ponce Perez, [b] O. Raymond Herrera [b] and J. Guerrero Sanchez *[b]

In the present work, we report the synthesis and detailed investigation on the structural, microstructural, and magnetic properties of ZnO–*x*Pt (*x* = 0.0, 0.02, 0.06, 0.10 wt%) nanocomposites, using experimental and theoretical approaches. The structural analysis, using Rietveld-refined X-ray diffraction patterns, shows that all samples exhibit a wurtzite phase with a hexagonal structure and a $P6_3mc$ symmetry. Transmission electron microscopy analysis revealed a consistent morphology for different Pt percentages, with nanoparticle diameters consistently less than 100 nm. Room-temperature magnetic measurements revealed superparamagnetic behavior, with the saturation magnetization increasing with the Pt percentage. However, the loops exhibited open regions in the low magnetic field range, where the remanent magnetization and coercivity also increased with the Pt weight percentage. The magnetic behavior is partly attributed to the bound magnetic polaron mechanism, and Thamm–Hesse analysis ruled out significant interparticle interactions, suggesting that clustering is not the dominant contribution. Density functional theory calculations indicate that Pt incorporation at Zn sites is energetically stable, regardless of the presence of oxygen vacancies. Spin-density isosurfaces reveal localized magnetic moments around Pt and adjacent oxygen atoms. The projected density of states exhibits a transition from semiconducting to half-metal behavior, producing spin-polarized carriers that can mediate long-range magnetic interactions. The close agreement between experimental observations and theoretical predictions highlights low-concentration Pt-doped ZnO as a promising nanoscale material for spintronic applications.

Received 12th October 2025,
Accepted 5th January 2026

DOI: 10.1039/d5tc03683f

rsc.li/materials-c

Introduction

Zinc oxide (ZnO) is well-known as a wide-bandgap semiconductor with a bandgap of 3.27–3.37 eV, characterized by a large exciton binding energy of 60 meV, which makes it a suitable material for application in optoelectronics, sensors, and ultraviolet light emitters.[1–8] The progress in diluted magnetic semiconductors (DMSs), which combine magnetic ordering with semiconducting behavior, is the center of attraction for spintronic devices. DMSs are a class of materials in which transition metals are introduced into the cationic sites to tailor their physical properties, and they are receiving significant attention due to their potential for application in spintronic devices.[9–11] Spintronics devices offer various benefits over traditional electronic devices, utilizing spin carriers to transport, store, and process information, instead of electrons as the primary charge carriers. However, in DMS-based devices, achieving long spin lifetimes and efficient spin injection and detection at room temperature is very challenging. It is a well-established fact that doping strategies are an effective way to alter physical properties, and in the case of ZnO, transition metal substitution has been explored to induce ferromagnetism in this material. Among these dopants, a noble metal (Pt) has emerged as a promising candidate due to its unique

[a] SECIHTI – IxM – Centro de Nanociencias y Nanotecnología, Universidad Nacional Autónoma de México, Km 107 Carretera Tijuana-Ensenada, AP 14, Ensenada 22800, B.C., México. E-mail: subhash@ens.cnyn.unam.mx
[b] Centro de Nanociencias y Nanotecnología, Universidad Nacional Autónoma de, MéxicoKm 107 Carretera Tijuana-Ensenada, AP 14, Ensenada 22800, B.C., México. E-mail: guerrero@ens.cnyn.unam.mx
[c] SECIHTI – IxM, Centro de Investigación en Materiales Avanzados, S.C., Miguel de Cervantes 120, Chihuahua, Chih, 31136, México
[d] Department of Physics & Environmental Sciences, Sharda School of Engineering & Science, Sharda University, Uttar Pradesh 201310, India
[e] Department of Chemistry, Himachal Pradesh University, Summer Hill, Shimla-5, Himachal Pradesh 171005, India

electronic configuration and potential to alter the carrier concentration and defects within the ZnO matrix.[12–15] Therefore, Pt addition on the ZnO surfaces is expected to induce weak ferromagnetic ordering, which is crucial for the development of spin-based devices. The weak ferromagnetic ordering in ZnO-based materials is attributed to the interaction of localized magnetic moments with conduction electrons, facilitated by lattice distortions and defect states induced by dopants.[13] Pt doping has also a center of attraction in recent times due to its sensing and photocatalytic properties; however, there are fewer reports in this direction, specifically regarding its magnetic properties.[15–17] The promising magnetic ordering at room temperature observed in Pt–ZnO nanomaterials opens new horizons for next-generation spintronic devices based on ZnO. Therefore, in the present work, we investigate these properties comprehensively, using the sol–gel route to prepare ZnO–*x*Pt nanocomposites for different values of *x*. The detailed structural analysis using X-ray diffraction (XRD), including Rietveld refinements, was performed to determine the correct lattice parameters. Magnetic properties are also discussed in detail for all studied samples. Furthermore, density functional theory (DFT) calculations were employed to understand the observed magnetic properties in the studied samples, revealing how the dopant-induced structural distortion influences the electronic band and, consequently, the magnetic behavior.[18–20]

Experimental and characterization section

The nanocomposites in the ZnO–*x*Pt system with x = 0.0, 0.02, 0.06, and 0.10 wt% (samples labeled as ZnO, Pt2, Pt6, and Pt10, respectively) were prepared by a simple, low-cost sol–gel route. The precursors, $Zn(NO_3)_2{\cdot}6H_2O$ (Merck, >99%), a 3 nm Pt nanoparticle dispersion in water at 1000 ppm (Sigma-Aldrich, 99.99%), and citric acid as a complexing agent ($C_6H_8O_7{\cdot}H_2O$, Merck, >99%), were used. An appropriate amount of Zn nitrate was dissolved in deionized water and stirred for 20–25 minutes on a magnetic stirrer, followed by the addition of an appropriate amount of Pt-sol. The citric acid was added in a 1 : 1 molar ratio of metal ion to citrate and kept at 70 °C on a hot plate with magnetic stirring for 2 hours. Then, a gel was obtained after 2 hours, followed by heating at ~110 °C in an oven for 12 hours to form a dry gel. Finally, the dry gel was ground to make a fine powder and subjected to calcination at 525 °C to promote the crystalline phase. An XRD diffractometer (Cu Kα radiation, λ = 1.5406 Å) was used to determine the crystal phase of the samples under study. Rietveld analysis was performed using FullProf software to determine the lattice parameters. The morphology was studied using scanning transmission electron microscopy (STEM), employing a Hitachi HT7700 microscope (EXALENS System) with operating voltages ranging from 40 to 120 kV and a maximum spatial resolution of 0.14 nm. A physical property measurement system (PPMS) with a VMS probe of Quantum Design was used to study the room-temperature (300 K) magnetic properties.

Computational methods

Spin-polarized total energy calculations within the framework of density functional theory were carried out using the Vienna *ab initio* simulation package (VASP).[21–24] Exchange and correlation effects were treated according to the generalized gradient approximation (GGA) with the Perdew–Burke–Ernzerhof (PBE) parametrization.[25] A plane-wave basis set with a cut-off energy of 400 eV was adopted to represent the electronic wavefunctions. The projector augmented wave (PAW) method was employed to account for the frozen-core approximation.[26,27] It is well-known that standard GGA and LDA approaches significantly underestimate the ZnO band-gap and its magnetic properties when doped with magnetic atoms.[26–30] Due to the highly localized nature of Zn 3d electrons, various functionals and correction methods have been proposed in recent studies to improve the accuracy of ZnO property descriptions. These include GGA+U,[31–33] LDA+U,[34] and hybrid functionals such as PBE0,[35] HSE,[36] and HSE06.[30] Among these approximations, the Hubbard correction is the most widely used due to its precision in describing magnetic properties and its lower computational cost compared to hybrid functionals or HSE approximations.[37–39] In this work, we adopted the DFT+*U* approach, applying the Hubbard correction as formulated by Dudarev *et al.*,[40] with a *U* parameter of 6 eV for Zn atoms, consistent with previous reports.[41–44] For Pt atoms, although they also present localized 5d electrons, previous DFT reports have shown that standard DFT calculations give excellent results.[43,44] The inclusion of the Hubbard correction does not significantly affect the magnetic properties of the Pt atoms. Additionally, our calculations confirm that the magnetic moment in Pt-doped ZnO arises primarily from the Pt atoms themselves, which induce a small magnetization in the neighboring O atoms even without applying the Hubbard correction on Pt. Thus, introducing a Hubbard correction on Pt atoms would not qualitatively change the magnetic behavior or the conclusions of this study. Structural optimization was achieved when the residual force on each atom was less than 0.01 eV Å^{-1}, and the total energy difference converged below 10^{-4} eV. Brillouin zone sampling was performed using a 3 × 3 × 2 Monkhorst–Pack *k*-point mesh.[45] To enhance the reliability of the simulations, the surface was modeled using the supercell method. A 3 × 3 × 3 periodic ideal hexagonal wurtzite supercell was employed to explore the effects on the magnetic properties of pristine ZnO, Zn and O vacancies, and Pt doping at Zn and O substitutional sites, as well as at interstitial positions. In addition to single Pt substitutions, a configuration with two Pt atoms substituting two Zn atoms was also considered. This configuration enables us to investigate the impact of Pt concentration on the magnetic moment. Increasing the number of Pt atoms beyond one would lead to a large number of possible configurations, making such an analysis beyond the scope of this work. Therefore, only one representative configuration with two Pt atoms was selected to illustrate the experimentally observed trend in magnetization.

Defect formation energy formalism

To investigate the thermodynamic stability of Pt incorporation into the ZnO matrix, the defect formation energy (DFE) formalism was employed. This approach, which is independent of the total number of atoms in the system, depends only on the chemical potentials (μ_i) of the constituent species. The formalism used here is adapted from previous studies[42,46,47] to suit the characteristics of our system. It is essential to assume thermodynamic equilibrium between the ZnO bulk and its constituents to apply the DFE formalism. This implies:

$$\mu_{Zn}^{bulk} + \mu_{O}^{molecule} - \Delta H_f^{ZnO} = \mu_{ZnO}^{bulk} = \mu_{Zn} + \mu_{O} \quad (1)$$

where ΔH_f^{ZnO} is the ZnO formation enthalpy and μ_i is the chemical potential. The calculated ΔH_f^{ZnO} value is −3.7 eV, which agrees with other reports.[41,48,49] Once thermodynamic equilibrium is considered, the DFE can be written as follows:

$$DFE = \frac{E_{sys} - E_{ref} - \Delta n_{Zn}\mu_{Zn} - \Delta n_{O}\mu_{O} - \Delta n_{Pt}\mu_{Pt}}{V} \quad (2)$$

where E_{sys} and E_{ref} are the total energy of the system under study and an arbitrary reference, respectively. Δn_i is the excess or deficit of the ith species in comparison with the reference, and μ_i is their corresponding chemical potential. To evaluate DFE, we vary the chemical potential from O-rich ($\mu_O = \mu_O^{molecule}$, $\mu_{Zn} = \mu_{Zn}^{bulk} - \Delta H_f^{ZnO}$) to O-poor conditions ($\mu_O = \mu_O^{molecule} - \Delta H_f^{ZnO}$, $\mu_{Zn} = \mu_{Zn}^{bulk}$). For the Pt impurities, we employed Pt-rich conditions ($\mu_{Pt} = \mu_{Pt}^{bulk}$) for the entire range of chemical potential.

Results and discussion

Structural properties

X-ray diffraction measurements were performed to determine the crystal structure and calculate the lattice parameters. All studied samples, after being calcined at 550 °C, were subjected to XRD analysis. Fig. 1a shows the XRD patterns, which clearly indicate the hexagonal wurtzite structure belonging to space group $P6_3mc$ as demonstrated by the observation of all standard planes [*i.e.*, (100), (002), (101), (102), (110), (103), (200), (112), and (201)] as per the JCPDS 079-2205 card.[4,9] It is worth noting that all samples exhibit a pure phase, with no other phases present. Furthermore, to calculate the lattice parameters, the Rietveld method was employed, as shown in Fig. 1b. The fitting parameters (*i.e.*, χ^2, R_p, and R_{wp}) are in an acceptable range, as shown in Table 1.

The lattice parameters and fitting parameters are listed in Table 1. It is found that the lattice parameters have no significant changes, as expected, since the Pt concentration is very low and the radius of the Pt^{2+} ions (0.60Å) is nearly the same as that of the Zn^{2+} ions (0.60Å) in four-coordination.[50] The average crystallite size was calculated for all samples from the XRD peak broadening using the Scherrer formula:[42,46]

$$D_{hkl} = \frac{K\lambda}{\beta_{hkl}\cos\theta_{hkl}}, \quad (3)$$

where K stands for the shape factor, λ stands for the used X-ray wavelength, β_{hkl} stands for the full width at half maxima (FWHM), and θ_{hkl} stands for the Bragg diffraction angle for each (hkl) plane.

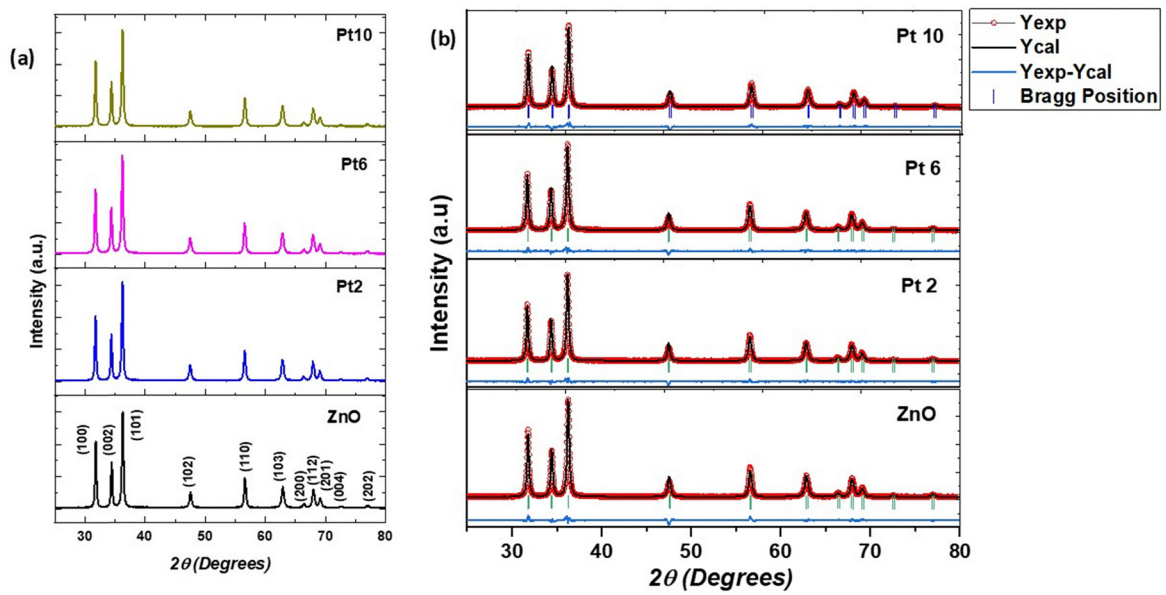

Fig. 1 (a) X-ray diffraction patterns and (b) Rietveld refined patterns for all ZnO–xPt samples with x = 0.00 (ZnO sample), 0.02 (Pt2), 0.06 (Pt6), and 0.10 (Pt10) wt%.

Table 1 Values of lattice parameters a and c, cell volume V_C, extracted fitting parameters (Rietveld-factors and χ^2), crystallite size D, distortion R, and microstrain η for all ZnO–xPt samples

wt% of Pt	a (Å)	c (Å)	V_C (Å^3)	Rietveld-factors	D (nm)	R	$\eta \times 10^{-3}$
0.00	3.2511	5.2099	47.6882	R_p = 6.96, R_{wp} = 9.12, R_{exp} = 5.33, χ^2 = 2.93	35	1.0190	1.52
0.02	3.2509	5.2094	47.6800	R_p = 6.70, R_{wp} = 8.55, R_{exp} = 5.37, χ^2 = 2.53	33	1.0190	1.30
0.06	3.2512	5.2105	47.6987	R_p = 6.92, R_{wp} = 8.86, R_{exp} = 5.39, χ^2 = 2.70	34	1.0189	1.10
0.10	3.2516	5.2108	47.7112	R_p = 7.25, R_{wp} = 8.93, R_{exp} = 5.41, χ^2 = 2.72	25	1.0190	1.10

To determine the strain in the samples, the Williams–Hall (W–H) approach was used as per the following relation:[51]

$$\beta_{hkl} = \frac{K\lambda}{D\cos\theta_{hkl}} + 4\eta\tan\theta_{hkl} \quad (4)$$

which can be rewritten as:

$$\beta_{hkl}\cos\theta_{hkl} = \frac{K\lambda}{D} + 4\eta\sin\theta_{hkl} \quad (5)$$

In this approach, the W–H method defines the two contributions to the broadening of the diffraction peak β_{hkl}: the first one (β_{size}) comes from crystallite size (*i.e.*, Scherrer formula), and the other one ($\beta_{strain} = 4\eta\tan\theta_{hkl}$) corresponds to microstrains due to crystal imperfections and distortions. Eqn (4) represents the uniform deformation model (UDM), assuming that the strain is uniform in all crystallographic directions.[49] Therefore, the plots of $\beta_{hkl}\cos\theta_{hkl}$ *vs.* $4\sin\theta_{hkl}$ have been graphed for each sample and are shown in Fig. 2. Using the linear fitting in the plots, the η and D values have been determined from the slope and the y-intercepts, respectively. The corresponding values are tabulated in Table 1. It is found that there is a decrease in strain, which may be attributed to the role of Pt incorporation in ZnO. The strain detected in the W–H analysis supports the presence of local lattice distortions, which, according to our DFT calculations (see the theoretical results section), play a central role in stabilizing the magnetic states upon Pt incorporation near oxygen vacancies. The crystal distortion induced by doping can be calculated as per the relation: $R = \frac{2a\sqrt{2/3}}{c}$, where a and c are the lattice constants. Thus, R describes the nature of the crystal structure, *i.e.*, indicates if the crystal structure is ideal or distorted, depending on the values of R (R = 1 for an ideal wurtzite

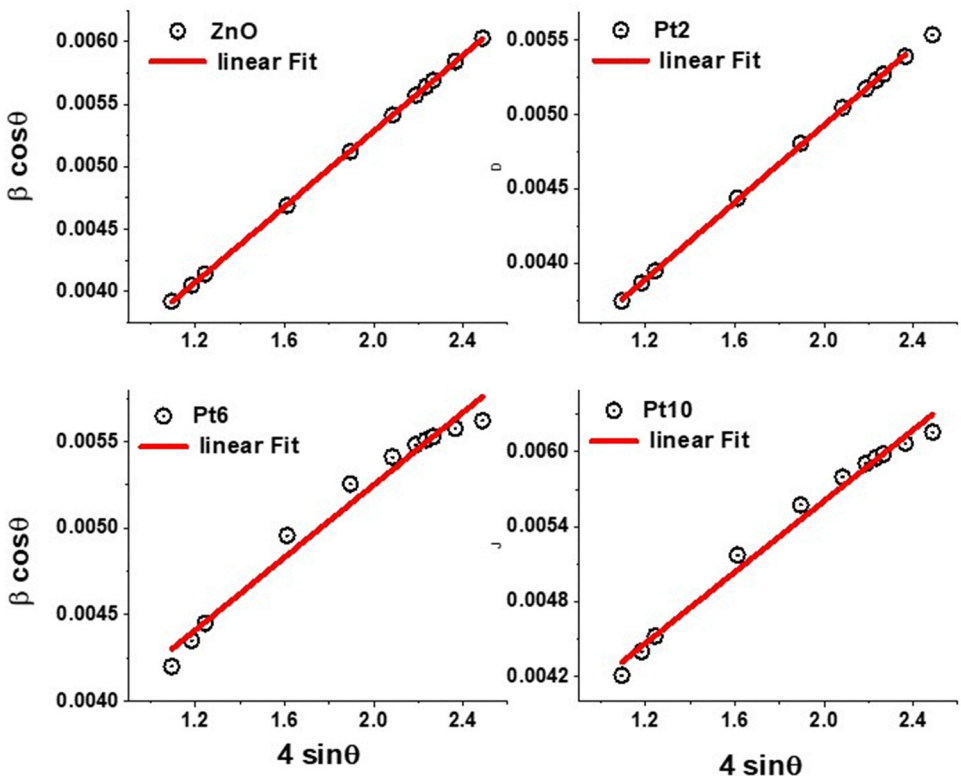

Fig. 2 The Williamson–Hall (W–H) plots for all ZnO–xPt samples with x = 0.00 (ZnO sample), 0.02 (Pt2), 0.06 (Pt6), and 0.10 (Pt10) wt%.

structure). In the present case, the value of R is very close to 1, indicating a nearly undistorted structure expected when the Pt content is very low.

The nanostructures exhibit a high degree of morphological uniformity, characterized by spherical and monodispersed particles across all Pt concentrations (Fig. 3(a–d)). This consistent morphology, irrespective of the Pt content, suggests that the synthesis process was highly controlled and reproducible. In support of this, the results of particle size distribution analysis are shown in Fig. 3(a–d), corresponding to ZnO–xPt particles with 0.00, 0.02, 0.06, and 0.10 wt% of Pt; the measured average particle sizes were 35.60 nm, 35.03 nm, 44.58 nm, and 44.00 nm, respectively. These values indicate relatively minor variation in particle size among samples with a low to moderate Pt content, highlighting the robustness of the synthesis procedure. The notable size reduction observed at 10 wt% of Pt may suggest a threshold concentration beyond which Pt influences nucleation dynamics. Particle sizes were statistically evaluated using ImageJ software, analyzing over 30 particles per sample. The size distributions were fitted to a Gaussian function, confirming a narrow dispersion and average diameters of less than 90 nm in most cases. This level of morphological precision is critical for applications such as photocatalysis and environmental remediation, where particle size and uniformity directly influence functional performance. These results demonstrate that the adopted synthetic strategy enables fine control over nanoparticle morphology and size, ensuring reproducibility and scalability for practical nanocomposite-based applications.

Magnetic properties

To investigate the magnetic properties, VSM measurements were performed at RT with applied magnetic fields in the range of +20 kOe to −20 kOe. Fig. 4a shows the RT magnetization curves as a function of the applied magnetic field (M–H curve) for all studied samples. As expected for ZnO (curve in the upper inset of Fig. 4a), a diamagnetic behavior is observed as reported by other researchers[10]; nevertheless, it exhibits a paramagnetic-like behavior close to zero magnetic field. Surprisingly, the ZnO–xPt samples show RT superparamagnetic behavior ascribed to single-domain ferromagnetic nanoparticles with a critical size.[52,53] Moreover, the magnetic saturation enhances with increasing concentration of Pt in the ZnO matrix. The bottom inset in Fig. 4a illustrates an opening of the M–H loop at the low magnetic field, suggesting a nonzero coercivity. The samples for x = 0.06 and 0.10 wt% show a saturated M–H curve, indicating that all magnetic moments are aligned at higher values of the magnetic field. The remanent magnetization is found to increase with increasing Pt content. In diluted magnetic semiconductors (DMS materials), the RT ferromagnetism remains poorly understood due to an incomplete understanding of whether it is an extrinsic effect resulting from direct interaction between the local moments in the magnetic impurity or an intrinsic property caused by exchange coupling between the spin of carriers and local moments.[42,46] The enhancement of ferromagnetism with Pt incorporation, together with the opening of the M–H loops, suggests that spin-polarized carriers mediate long-range interactions between localized Pt moments, as observed in N-doped ZnO.[54] Thamm–Hesse analysis was conducted to determine the type of such magnetic interactions between nanoparticles.

The Thamm–Hesse method (THM) is based on analyzing the difference ΔM between the initial magnetization curve and the average of the upper and lower branches of the hysteresis loop for systems composed of single-domain particles.[44–46] In this approach, the M–H curve is segmented into five regions of the applied magnetic field: (I) from 0 → H_{max} (initial magnetization curve);

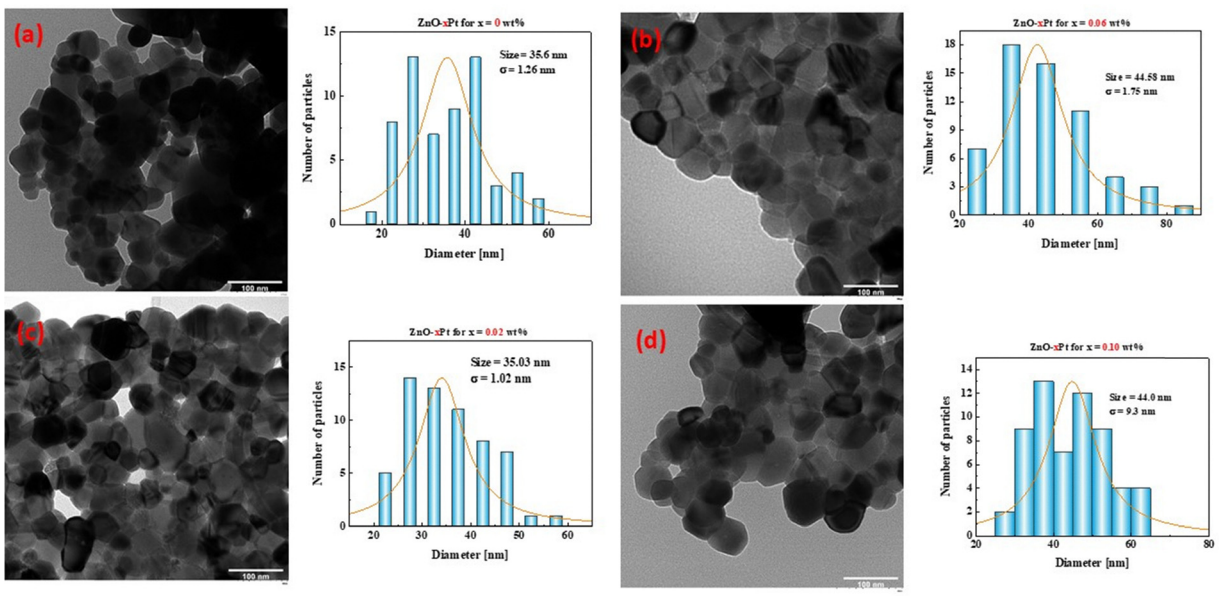

Fig. 3 Transmission electron microscopy micrographs and size distribution of ZnO–xPt nanocomposites synthesized with varying Pt wt% of (a) 0, (b) 0.02, (c) 0.06, and (d) 0.10.

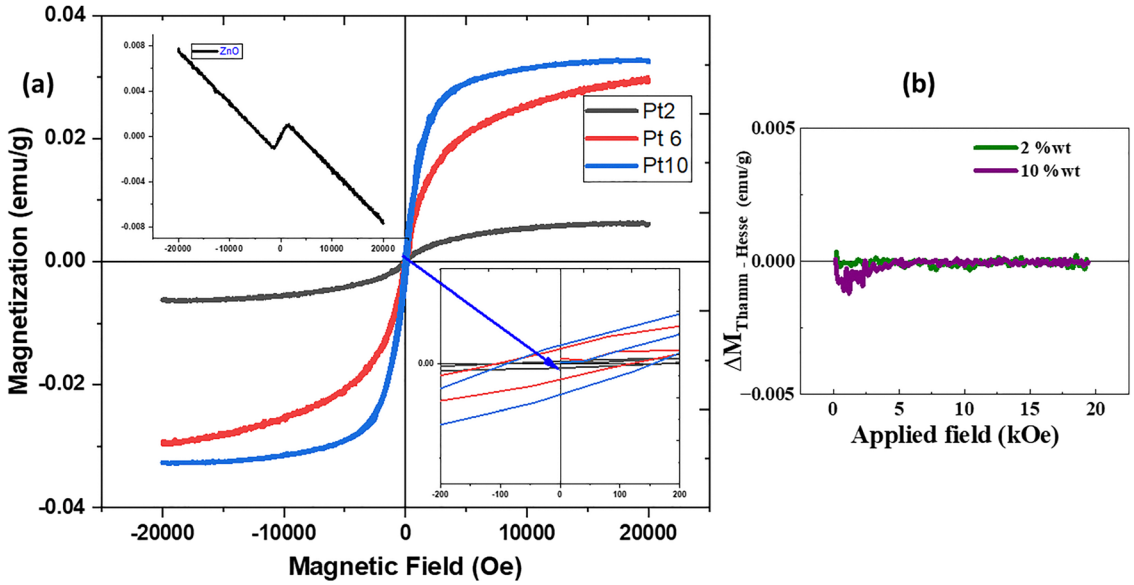

Fig. 4 (a) RT magnetization curve as a function of the applied magnetic field (*M vs. H*) for ZnO–*x*Pt with *x* = 0.00 (ZnO sample, in the upper inset), 0.02 (Pt2), 0.06 (Pt6), and 0.10 (Pt10) wt%. The lower inset shows a close-up view of the low-magnetic-field region. (b) Thamm–Hesse plots of the deviation Δ*M* as a function of the applied magnetic field for Pt2 and Pt10 samples.

(II) from $H_{max} \rightarrow 0$ (positive descending branch); (III) from $0 \rightarrow -H_{max}$ (excluded); (IV) from $-H_{max} \rightarrow 0$ (excluded); and (V) from $0 \rightarrow H_{max}$ (ascending branch). Only segments I, II, and V are considered for the analysis. Thus, the deviation Δ*M* from ideal behavior is calculated using the following expression:

$$\Delta M(H)_{\text{Thamm–Hesse}} = M_0 - \frac{M_{\text{upper}} + M_{\text{bottom}}}{2} \qquad (6)$$

where M_0 is the magnetization along the initial magnetization curve, M_{upper} and M_{bottom} correspond to the magnetization values obtained from the segments II and V, respectively. According to the Stoner–Wohlfarth model, which describes ideal non-interacting single-domain particles with uniaxial anisotropy undergoing coherent magnetization rotation, Δ*M* should be close to zero.[44–46] This condition suggests superparamagnetic or paramagnetic behavior, indicating negligible magnetic interactions between particles. Deviations from zero reveal the presence of one type of interparticle magnetic interaction. Thus, $\Delta M \approx 0$ means non-interacting particles (superparamagnetic or paramagnetic behavior); if $\Delta M > 0$, there is a predominance of exchange interactions that favor magnetization alignment; and if $\Delta M < 0$, we are in the presence of dipolar interactions that promote magnetization reversal. Consequently, the THM plot serves as a diagnostic tool to determine the nature and strength of interparticle magnetic interactions in nanoscale systems.

Fig. 4b presents the $\Delta M_{\text{Thamm–Hesse}}$ plots for ZnO–*x*Pt nanocomposites synthesized with *x* = 0.02 and 0.10 wt%, as a function of the applied magnetic field. The nearly zero Δ*M* values observed across the applied magnetic field range for both Pt concentrations indicate minimal interaction between magnetic domains, consistent with isolated single-domain behavior. Thus, the values of $\Delta M \approx 0$ confirm the superparamagnetic behavior, observed in the *M*–*H* curves, characteristic of the single-domain non-interacting particles. Additionally, a slight negative deviation is observed at low magnetic fields, more pronounced for 10 wt% Pt, indicating the presence of dipolar interactions that promote magnetization reversal, possibly due to the closer proximity of magnetic Pt domains or a higher density of magnetic centers.[55–57] All this suggests that ZnO–*x*Pt nanoparticles are magnetically isolated, and the magnetic interactions between them are negligible.

On the other hand, several theories have been proposed over time by various researchers, especially to explain the origin of the observed magnetic behavior of DMS materials, including carrier-mediated exchange interactions (RKKY), bound magnetic polarons (BMP) linked with oxygen-vacancy trapped carriers, double-exchange or super exchange between transition-metal ions, and the defect-induced magnetism (DIM) arising from intrinsic vacancies or non-stoichiometry.[1–8] Collectively, these mechanisms account for the diverse magnetic responses, ranging from weak ferromagnetism to superparamagnetic, commonly reported in doped and defect-engineered ZnO.[1–8] Notably, it is well-known that ZnO-based materials are characterized by the presence of oxygen vacancies, which lead to the formation of free localized electrons. Thus, a possible mechanism to explain the observed superparamagnetic behavior coming from ferromagnetic nanoparticles with a critical size is to consider the BMP model. The BMP model suggests that magnetic moments from dopant ions become aligned when they are trapped around localized charge carriers (usually electrons bound to oxygen vacancies). When several such defect–carrier complexes overlap, they form percolating magnetic clusters, giving rise to long-range ferromagnetism in dilute magnetic oxides.[11]

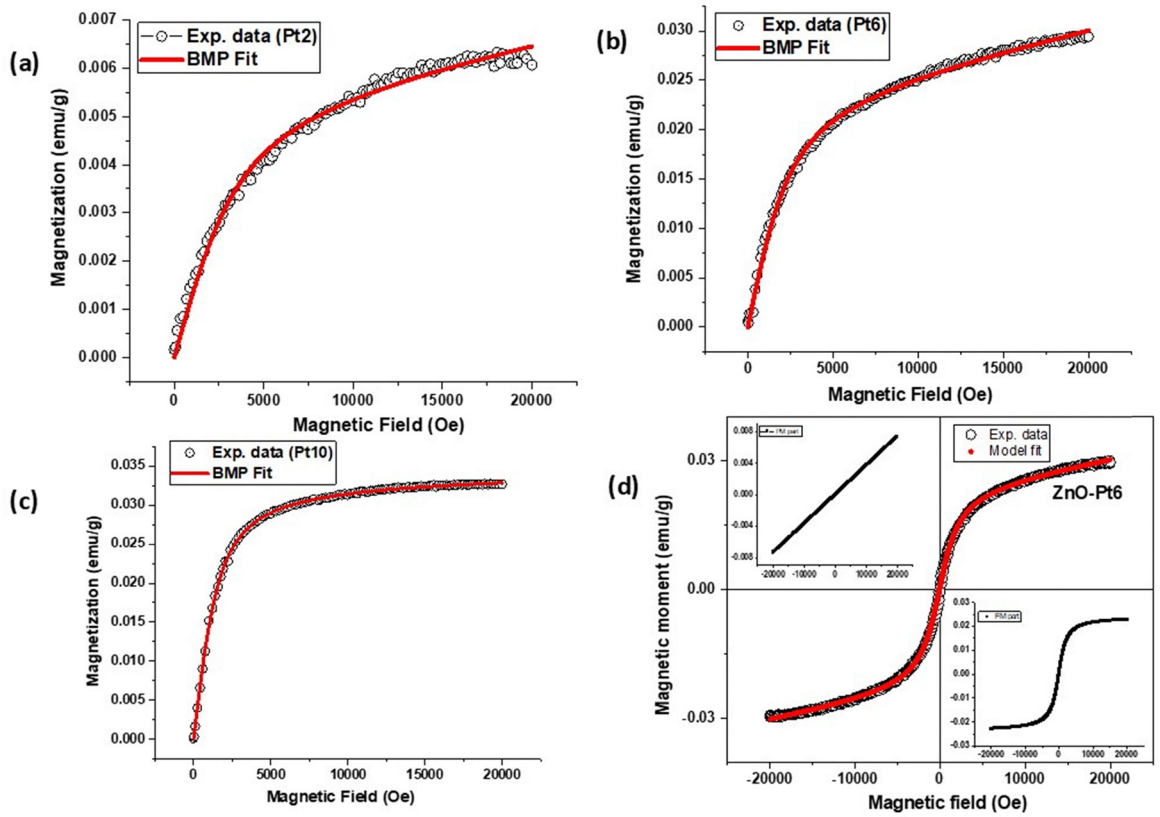

Fig. 5 BMP model fit of magnetization for values of Pt wt% of (a) x = 0.02 (Pt2), (b) x = 0.06 (Pt6), and (c) x = 0.10 (Pt10). (d) Fit of the M–H data using eqn (8) for x = 0.06 (Pt6), with the deconvoluted contributions of the paramagnetic (upper inset) and ferromagnetic (bottom inset) behaviors.

Table 2 The magnetic parameters using the BMP model and eqn (7) for the deconvolution of magnetic data for FM and PM contributions, and experimental magnetic parameters of the studied ZnO–xPt samples

	BMP model				Experimental parameters	
Pt wt%	M_o (10^{-3}) (emu g^{-1})	m_{eff} (10^{-18}) (emu)	N (cm^{-3})	χ (10^{-7}) (cgs)	M_r (10^{-4}) (emu g^{-1})	H_c (Oe)
x = 0.02	5.39	1.83	5.25×10^{14}	7.20	3.74	137
x = 0.06	23.63	2.66	1.58×10^{15}	3.97	16.4	113
x = 0.10	33.4	0.383	1.55×10^{16}	3.00	26.4	123

Therefore, we carried out the theoretical fit for the experimental M–H data to the following equation:[9,10]

$$M = M_o L(x) + \chi_m H \quad (7)$$

In eqn (7), the first term denotes the BMP contribution, and the second term is due to the observed paramagnetic part at a higher field; $M_o = N \times m_s$, where N is the number of BMP involved, and m_s denotes the effective spontaneous moment per BMP. $L(x) = \coth(x) - 1/x$ denotes the Langevin function with $x = m_{eff}H/(k_BT)$, where m_{eff} is the true magnetic spontaneous moment per BMP; at higher temperatures, the interactions between BMP can be avoided, and in that situation, $m_s = m_{eff}$. χ_m is the susceptibility of the BMP matrix. In the fitting process, M_o, m_{eff}, and χ_m are variables. As shown in Fig. 5(a–c), the initial M–H data are in good agreement with the BMP model. The extracted parameters are tabulated in Table 2. It is found that the number of BMPs is 5.25×10^{14}, 1.58×10^{15}, and 1.55×10^{16} per cm^3 for the Pt2, Pt6, and Pt10 samples, respectively. It is well-known that these ranges (*i.e.*, 10^{14}–10^{16} per cm^3) are not good enough for making a contribution to magnetism. The required concentration for significant percolation of BMPs is in the range of 10^{20} per cm^3.[58] Therefore, it is not fully manifested by BMP-mediated magnetism.

To explain the possible magnetic behavior in more depth, we carried out DFT calculations and have discussed the results in the following section. Furthermore, we extracted the paramagnetic (PM) and ferromagnetic (FM) contributions from the M–H curve using a fitting function by the following equation[59]:

$$M(H) = \left[2\frac{M_{FM}^S}{\pi}\tan^{-1}\left\{\left(\frac{H \pm H_{ci}}{H_{ci}}\right)\tan\left(\frac{\pi M_{FM}^R}{2M_{FM}^S}\right)\right\}\right] + \chi H \quad (8)$$

Here, χ is the magnetic susceptibility of the PM contribution. In eqn (8), the first term on the right-hand side, M_{FM}^{S}, denotes the ferromagnetic saturation magnetization, M_{FM}^{R} is the remnant magnetization, and H_c is the intrinsic coercivity. Fig. 5d shows the fitted M–H data to eqn (8) with PM and FM contributions for the Pt6 sample. It is observed from the fitting and the difference between experimental and theoretical parameters that the observed magnetic properties are purely FM in nature due to very little contribution from PM.

Theoretical results

The calculated lattice parameters of pristine ZnO are a = 3.20 Å and c = 5.16 Å, with a Zn–O bond length of 1.95 Å. These values are consistent with previous reports and our experimental results.[25,38,49,60] For reference, the ZnO-(3 × 3 × 3) supercell and its projected density of states (PDOS) are shown in Fig. 6. According to the PDOS, ZnO does not exhibit magnetic properties since the spin-up and spin-down states are symmetric, indicating a magnetic null moment, and a bandgap of approximately 1.58 eV, in good agreement with previous reports.[38] The valence band is mainly composed of O-2p orbitals, while the Zn-3d orbitals also contribute. In the conduction band, both elements contribute equally. For Pt atoms, although they also present localized 5d electrons, previous DFT reports have shown that standard DFT calculations give excellent results.[43,44]

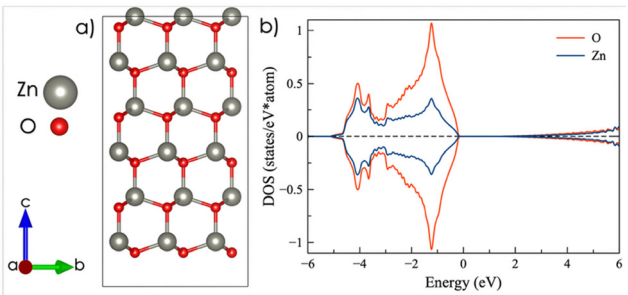

Fig. 6 (a) Atomistic model of the ZnO-(3 × 3 × 3) supercell and (b) the corresponding PDOS for Zn and O. The Fermi level is set to zero. Positive values correspond to spin-up and negative values to spin-down.

We employed the DFE formalism to analyze the thermodynamic stability of ZnO doped with Pt atoms under different chemical potential conditions. Four doping configurations were considered, as shown in Fig. 7: (a) Pt substituting a Zn atom, (b) Pt substituting an O atom, (c) Pt replacing a Zn atom with an adjacent O vacancy, and (d) Pt occupying an interstitial site. Fig. 7(f) displays the 2D DFE plot under O-poor to O-rich conditions. The energy reference corresponds to the pristine ZnO-(3 × 3 × 3) system.

According to the DFE formalism, the most thermodynamically favorable (*i.e.*, experimentally probable) configurations are those with the lowest DFE values. Negative DFE values indicate spontaneous reactions, while positive values denote non-spontaneous processes. Our results show that the most stable structure for all chemical potential ranges is the two Zn substitution with an O vacancy (purple line), followed by the O substitution (red line) under O-poor to O-intermediate conditions, whereas the one Zn substitution with an O vacancy becomes stable under O-intermediate to O-rich conditions (blue line), demonstrating that the doping substitution with and without O vacancies is the most probable experimentally. Our results show that the most stable structure under O-poor to O-intermediate conditions is the O substitution (red line), whereas the Zn substitution becomes stable under O-intermediate to O-rich conditions (blue line). Interestingly, under intermediate conditions, a triple point involving O substitution, Zn substitution, and Zn substitution with an O vacancy is observed (green line), as shown in Fig. 7e. Additionally, the interstitial Pt configuration is more stable than the pristine system. These findings are consistent with previous theoretical studies suggesting that ZnO structures with vacancies are more stable than the pristine material, making it feasible to introduce doping atoms into the ZnO matrix.[43,61] In all cases, the energy differences are less than 0.004 eV Å^{-3}, suggesting that all these configurations are experimentally feasible.

Furthermore, we calculated the Bader charge transfer to evaluate the interactions among the atomic species. In bare

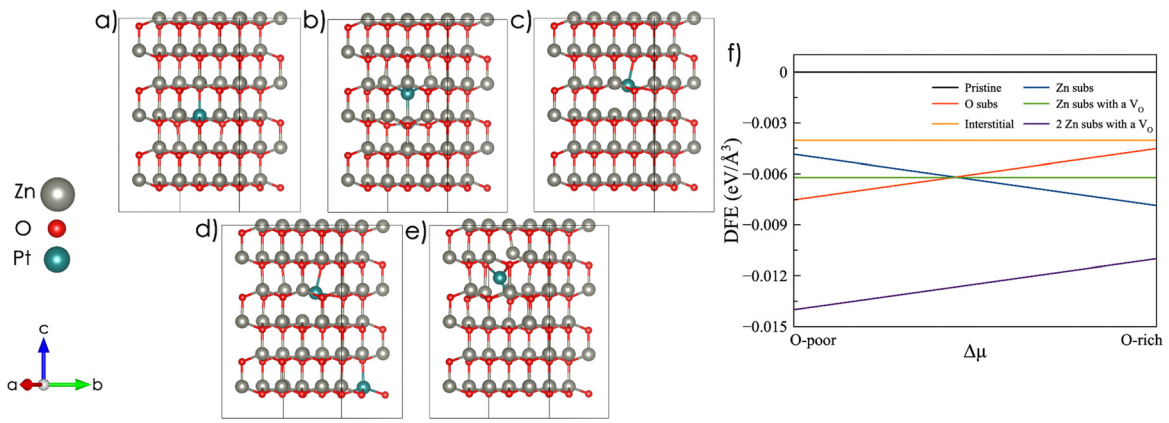

Fig. 7 Atomistic models of Pt-doped ZnO: (a) Zn substitution, (b) O substitution, (c) Zn substitution with an O vacancy, (d) two Zn substitutions with an O vacancy, and (e) interstitial site. (f) The DFE energy plot. The O-poor chemical potential is −8.397 eV, and under O-rich conditions, it is −4.647 eV.

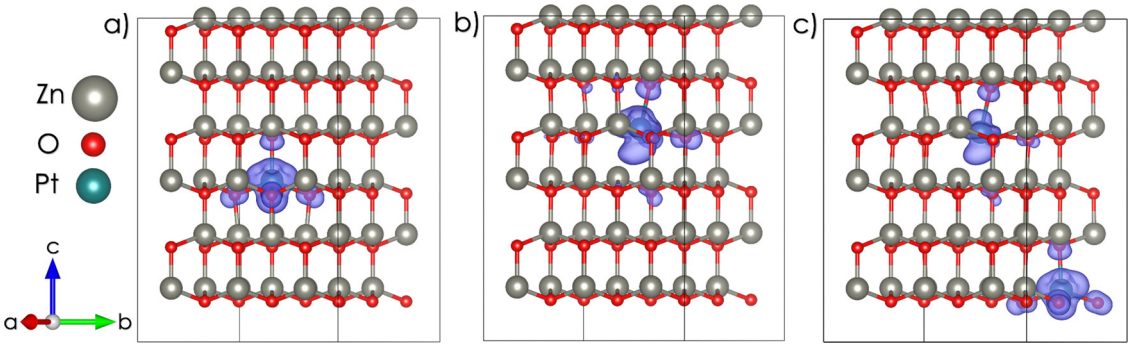

Fig. 8 Spin-density isosurfaces for the Zn substitution configurations: (a) a Pt atom without an O vacancy, (b) a Pt atom with an O vacancy, and (c) two Pt atoms.

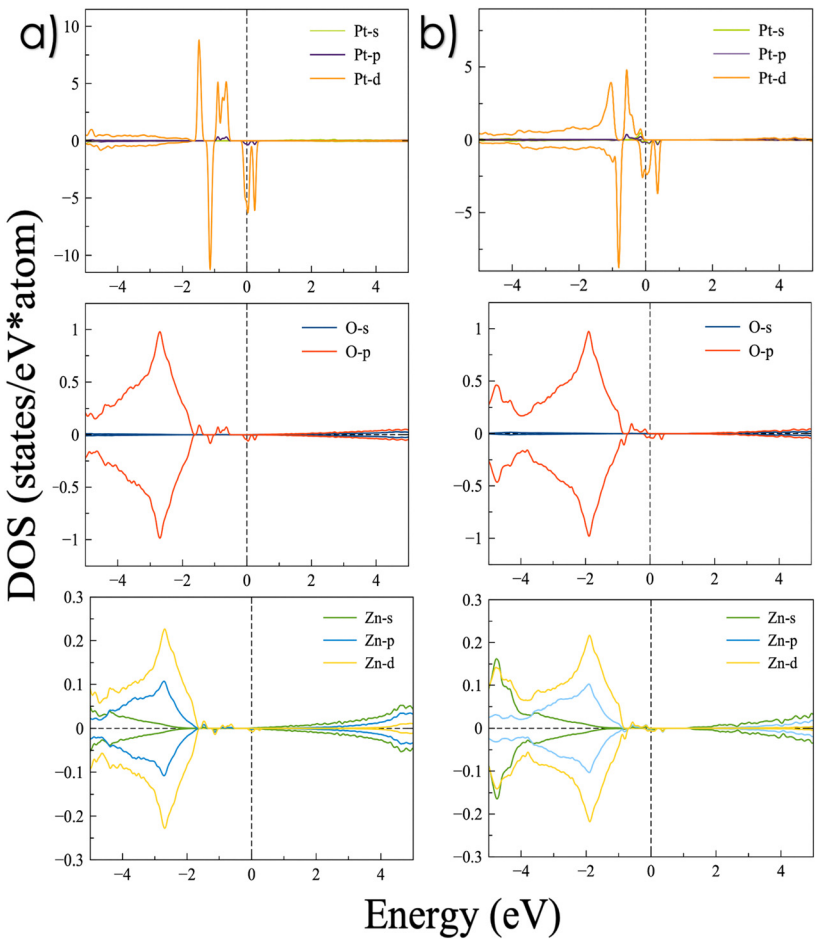

Fig. 9 Orbital-resolved densities of states for the Zn substitution configurations: (a) without an O vacancy and (b) with an O vacancy.

ZnO, Zn atoms donate 1.18e, while O atoms gain −1.18e, confirming that Zn acts as a donor and O as an acceptor. In the O substitution system, Pt has a charge transfer of −0.74e, acting as an acceptor or anion. In the Zn substitution system, Pt donates 0.70e, acting as a donor or cation. In the interstitial system, Pt shows a negligible charge transfer of −0.06e; in the Zn substitution with an O vacancy with one and two Pt atoms, Pt shows a transfer of 0.07e. In the last two cases, the minimal charge transfer suggests that Pt remains in its metallic state.

According to our experimental results, Pt atoms induce magnetism in the ZnO matrix. To investigate the origin of the magnetic properties in Pt-doped systems, we calculated the spin-density isosurfaces (Fig. 8) and the PDOS (Fig. 9) exclusively for the Zn substitution and for the O vacancy

configuration with one and two Pt atoms, as these are the only systems that exhibit a significant and localized magnetic moment. The negligible interparticle interaction observed in the THM analysis is consistent with our localized magnetization at the Pt atom and nearby O, rather than delocalized on the ZnO lattice.

The spin-density isosurfaces reveal that the Pt atom exhibits local magnetization in all configurations, with nearby oxygen atoms showing weakly induced magnetization. The total magnetic moments are as follows: $1.87\mu_B$ for one Zn substitution, $3.75\mu_B$ for two Zn substitutions, $0.12\mu_B$ for O substitution, $0.23\mu_B$ for interstitial Pt, and $1.84\mu_B$ for Zn substitution with an O vacancy. This trend in total magnetization aligns well with the observed increase in magnetic saturation as the Pt content increases in the ZnO matrix. The orbital-resolved PDOS for all Zn substitutional systems confirms the emergence of ferromagnetism and a transition from semiconducting to half-metallic behavior. The spin-up states near the Fermi level are mainly associated with Pt atoms, while impurity states at the Fermi level for the spin-down channel originate primarily from the Pt-d and -p orbitals, which are responsible for the half-metallic character of Pt-doped ZnO (see Fig. 9). Additionally, the O-p orbitals of neighboring O atoms contribute to the magnetic behavior through induced spin polarization caused by their proximity to Pt, representing the third most relevant contribution to the magnetic transition. In contrast, Zn atoms have a negligible effect on magnetization, with their electronic states lying predominantly at negative energy levels. The same tendency is found for the substitution of two Zn atoms with one O vacancy.

Combining all the experimental and theoretical evidence, we see that magnetism in ZnO cannot be explained by BMP contributions or clustering effects. While BMP fitting accounts only for part of the magnetic response, the estimated polaron density is insufficient to explain the observed magnetism. Additionally, THM analysis confirms small or negligible particle interactions, eliminating the possibility of clustering formation, which is also supported by the XRD measurements showing no extra phases. The enhancement of ferromagnetism with Pt doping points to other mechanisms. Our theoretical calculations helped us understand this behavior, revealing that Pt substitution at Zn sites drives a semiconductor to a half-metal transition, with spin asymmetry at the Fermi level. This electronic character partially explains the magnetism observed in the experimental loops, as spin-polarized carriers mediate the long-range interactions between the localized Pt atom moments, possibly giving rise to the enhanced magnetism observed at higher Pt concentrations.

Conclusions

Here, we successfully synthesized Pt-doped ZnO nanomaterials using the sol–gel method and systematically studied their structural, microstructural, and magnetic properties, supported by density functional theory calculations. XRD with Rietveld analyses confirmed that all samples have a wurtzite structure with uniform particle morphology. Additionally, Williamson–Hall analysis indicated local lattice distortions caused by Pt incorporation. Magnetic measurements revealed superparamagnetic behavior at room temperature, characterized by a consistent increase in remnant magnetization and loop saturation as the Pt concentration increased. The Bound Magnetic Polaron model explains part of the magnetic response, while the Thamm–Hesse method excluded significant interparticle interactions, suggesting that clustering is not a dominant mechanism. Our theoretical results offer a detailed atomic-scale explanation of these findings. The stability analysis revealed that Pt incorporation remains stable in Zn sites, regardless of the presence of O vacancies. Spin density isosurfaces displayed localized magnetic moments around the Pt and neighboring O atoms, and the projected density of states confirmed the transition from semiconductor to half-metal. These electronic properties show clear spin-polarized carriers, which could mediate long-range interactions between localized Pt moments. Finally, the experimental results align with the theoretical predictions, showing an increase in magnetization as Pt concentration increases, making low-concentration Pt-doped ZnO a promising candidate for spintronics devices with tailored properties at the nanoscale.

Conflicts of interest

The authors declare that they have no known competing financial interests or personal relationships that could have appeared to influence the work reported in this paper.

Data availability

All the data in this study are within the paper.

Acknowledgements

This work was partially supported by DGAPA-UNAM, through research Grants DGAPA-PAPIIT IT100525, IA100226, IN110424, and IG101124. Calculations were performed in the DGCTIC-UNAM Supercomputing Center *via* projects LANCAD-UNAM-DGTIC-452, 150, 286, 368, 422, and 457. The authors would like to thank Pedro Casillas, Luis Alejandro Arce Saldaña, Aldo Rodriguez, Luis Angel De Leon Alanis, and Samuel Flores Garcia, for their valuable technical support. Subhash Sharma and Javier Alonso Lxopez Medina acknowledge support from the SECIHTI Program *via* the Researchers for Mexico initiative through Projects 352-2018 and 146–2016, respectively. C. A. Corona-García thanks DGAPA-UNAM for the postdoctoral grant.

References

1 Ü. Özgür, *et al.*, A comprehensive review of ZnO materials and devices, *J. Appl. Phys.*, 2005, **98**, 041301.

2 D. C. Look, Recent advances in ZnO materials and devices, *Mater. Sci. Eng. B*, 2001, **80**, 383–387.
3 I. Jabbar, *et al.*, Diluted magnetic semiconductor properties in TM-doped ZnO nanoparticles, *RSC Adv.*, 2022, **12**, 13456–13463.
4 A. Sukumaran and N. Gopalakrishnan, Donor-defect-induced ferromagnetism in Nb-doped ZnO thin films grown by RF magnetron sputtering, *Phys. Status Solidi A*, 2024, **221**, 2400219.
5 M. Mohamed, A. Sedky and M. S. Alshammari, An investigation on structural, optical, and magnetic properties of $Zn_{1-x}Co_xO$ nanorods fabricated by electrochemical deposition, *Sci. Rep.*, 2025, **15**, 37947.
6 N. Ali, B. Singh, A. R. Vijaya, S. Lal, C. S. Yadav, K. Tarafder and S. Ghosh, Ferromagnetism in Mn-doped ZnO: A joint theoretical and experimental investigation, *J. Phys. Chem. C*, 2021, **125**, 7734–7745.
7 R. Khan, *et al.*, Room-temperature dilute magnetic semiconductor behavior in co-doped (Gd/Co etc.) ZnO nanotubes and related systems, *RSC Adv.*, 2022, **12**, 36126–36137.
8 M. A. Wahb, Robust ferromagnetic V0.05-XCoxZn0.95O (x = 0.01, 0.02, 0.03, 0.04, 0.05) nano-compounds: New dilute magnetic-semiconductors with tailored optical activity, *J. Magn. Magn. Mater.*, 2024, **25**, 175503.
9 T. Dietl, *et al.*, Zener model description of ferromagnetism in zinc-blende magnetic semiconductors, *Science*, 2000, **287**, 1019–1022.
10 G. Srinet, R. Kumar and V. Sajal, Structural, optical, vibrational, and magnetic properties of sol-gel derived Ni doped ZnO nanoparticles, *J. Appl. Phys.*, 2013, **114**, 033912.
11 B. Pal and P. K. Giri, High temperature ferromagnetism and optical properties of Co doped ZnO nanoparticles, *J. Appl. Phys.*, 2010, **108**, 084322.
12 S. J. Pearton, *et al.*, Recent progress in processing and properties of ZnO, *Superlattices Microstruct.*, 2003, **34**, 3–32.
13 M. Venkatesan, *et al.*, Unexpected magnetism in a dielectric oxide, *Nature*, 2004, **430**, 630.
14 S. B. Patil, G. E. Patil and P. V. Dalal, Enhanced gas sensing performance of ZnO and Pt-doped ZnO nanostructured films by chemical spray pyrolysis, *Surf. Interfaces*, 2024, **54**, 105173.
15 A. Mezn, *et al.*, Pt–ZnO/M (M = Fe, Co, Ni or Cu): A New Promising Hybrid-Doped Noble Metal/Semiconductor Photocatalysts, *J. Inorg. Organomet. Polym. Mater.*, 2020, **30**, 4627–4636.
16 J. Rodríguez-Carvajal, Recent advances in magnetic structure determination by neutron powder diffraction, *Physica B*, 1993, **192**, 55–69.
17 J. A. L. Medina, *et al.*, ZnO@Pt nanocomposites for enhanced amaranth dye degradation under UV–vis irradiation, *Appl. Surf. Sci.*, 2026, **716**, 164715.
18 P. Hohenberg and W. Kohn, Inhomogeneous electron gas, *Phys. Rev.*, 1964, **136**, B864.
19 Q. L. Lin, *et al.*, First-principles study of defect-induced ferromagnetism in ZnO, *J. Chem. Phys.*, 2019, **150**, 094704.
20 G. Kresse and J. Hafner, Ab initio molecular dynamics for liquid metals, *Phys. Rev. B:Condens. Matter Mater. Phys.*, 1993, **47**, 558.
21 G. Kresse and J. Hafner, Ab initio molecular-dynamics simulation of the liquid-metal-amorphous-semiconductor transition in germanium, *Phys. Rev. B:Condens. Matter Mater. Phys.*, 1994, **9**, 14251.
22 G. Kresse and J. Furthmüller, Efficiency of ab-initio total energy calculations for metals and semiconductors using a plane-wave basis set, *Comput. Mater. Sci.*, 1996, **6**(1), 15–50.
23 G. Kresse and J. Furthmüller, Efficient iterative schemes for ab initiototal-energy calculations using a plane-wave basis set, *Phys. Rev. B:Condens. Matter Mater. Phys.*, 1996, **54**, 11169.
24 J. P. Perdew, K. Burke and M. Ernzerhof, Generalized Gradient Approximation Made Simple, *Phys. Rev. Lett.*, 1996, **77**, 3865.
25 P. E. Blöchl, Projector augmented-wave method, *Phys. Rev. B:Condens. Matter Mater. Phys.*, 1994, **50**, 17953.
26 G. Kresse and D. Joubert, From ultrasoft pseudopotentials to the projector augmented-wave method, *Phys. Rev. B:Condens. Matter Mater. Phys.*, 1999, **59**, 1758.
27 S. Lardjane, G. Merad, N. Fenineche, A. Billard and H. I. Faraoun, Ab initio study of ZnCoO diluted magnetic semiconductor and its magnetic properties, *J. Alloys Compd.*, 2013, **551**, 306–311.
28 P. Sikam, P. Moontragoon, J. Jumpatam, S. Pinitsoontorn, P. Thongbai and T. Kamwanna, Structural, Optical, Electronic and Magnetic Properties of Fe-Doped ZnO Nanoparticles Synthesized by Combustion Method and First-Principle Calculation, *J. Supercond. Novel Magn.*, 2016, **29**, 3155–3166.
29 P. Moontragoon, S. Pinitsoontorn and P. Thongbai, Mn-doped ZnO nanoparticles: Preparation, characterization, and calculation of electronic and magnetic properties, *Microelectron. Eng.*, 2013, **108**, 158–162.
30 M. V. Gallegos, C. R. Luna, M. A. Peluso, L. C. Damonte, J. E. Sambeth and P. V. Jasen, Effect of Mn in ZnO using DFT calculations: Magnetic and electronic changes, *J. Alloys Compd.*, 2019, **795**, 254–260.
31 E. Ozugurlu, Cd-doped ZnO nanoparticles: An experimental and first-principles DFT studies, *J. Alloys Compd.*, 2021, **861**, 158620.
32 F. Maldonado, L. Villamagua and R. Rivera, DFT Analysis of the Adsorption of Phenol on the Nonpolar (1-010) ZnO Surface, *J. Phys. Chem. C*, 2019, **123**, 12296–12304.
33 A. Janotti and C. G. Van de Walle, Oxygen vacancies in ZnO, *Appl. Phys. Lett.*, 2005, **87**, 122102.
34 S. Masoumi, E. Nadimi and F. Hossein-Babaei, Electronic properties of Ag-doped ZnO: DFT hybrid functional study, *Phys. Chem. Chem. Phys.*, 2018, **20**, 14688.
35 K. Qi, X. Xing, A. Zada, M. Li, Q. Wang, S. Liu, H. Lin and G. Wang, Transition metal doped ZnO nanoparticles with enhanced photocatalytic and antibacterial performances: Experimental and DFT studies, *Ceram. Int.*, 2020, **46**, 1494–1502.
36 E. Mamani-Flores, M. L. Moreira and M. Jeomar-Piotrowski, Structural and Electronic Properties of Bulk ZnX (X = O, S, Se, Te), ZnF2 and ZnO/ZnF2: A DFT Investigation within PBE, PBE + U, and Hybrid HSE Functionals, *J. Phys. Chem. A*, 2020, **124**(19), 3778–3785.

37 D. S. Lambert and D. D. O'Regan, Use of DFT+U + J with linear response parameters to predict non-magnetic oxide band gaps with hybrid-functional accuracy, *Phys. Rev. Res.*, 2023, **5**, 013160.
38 W. Li, X. Xin, H. Wang, C. Guo, H. Jiang and Y. Zhao, Description of light-element magnetic systems via density functional theory plus U with an example system of fluorinated boron nitride: An efficient alternative to hybrid functional approach, *Comput. Mater. Sci.*, 2018, **146**, 84–89.
39 S. L. Dudarev, G. A. Botton, S. Y. Savrasov, C. J. Humphreys and A. P. Sutton, Electron-energy-loss spectra and the structural stability of nickel oxide: An LSDA + U study, *Phys. Rev. B:Condens. Matter Mater. Phys.*, 1998, **57**, 1505.
40 M. V. Gallegos, C. R. Luna, M. A. Peluso, L. C. Damonte, J. E. Sambeth and P. V. Jasen, Effect of Mn in ZnO using DFT calculations: Magnetic and electronic changes, *J. Alloys Compd.*, 2019, **795**, 254–260.
41 A. Walsh, J. L. F. Da Silva and S.-H. Wei, Theoretical Description of Carrier Mediated Magnetism in Cobalt Doped ZnO, *Phys. Rev. Lett.*, 2008, **100**, 256401.
42 S. Sharma, R. Ponce-Pérez, M. G. Moreno-Armenta, J. Guerrero-Sánchez, R. Kumar, S. Kumar, J. M. Siqueiros and O. Raymond-Herrera, An Atomic-Scale Justification for the Weak Ferromagnetism Observed in Nanostructured Zn0.96-xCoxMn0.04 Powders, *J. Phys. Chem. C*, 2024, **128**, 11835–11844.
43 N. Seriani, Z. Jin, W. Pompe and L. Colombi Ciacchi, Density functional theory study of platinum oxides: From infinite crystals to nanoscopic particles, *Phys. Rev. B:Condens. Matter Mater. Phys.*, 2007, **76**, 155421.
44 W. E. I. Han, *et al.*, DFT Study on Electronic Interactions of Pt, Pd and Au Atoms with γ-Al2O3, *Mater. Sci.*, 2018, **24**(3), 239–242.
45 H. J. Monkhorst and J. D. Pack, Special points for Brillouin-zone integrations, *Phys. Rev. B*, 1976, **13**, 5188.
46 G. Srinet, S. Sharma, J. Guerrero-Sanchez, R. Garcia-Diaz, R. Ponce-Perez, J. M. Siqueiros and O. Raymond Herrera, Room-temperature ferromagnetism on ZnO nanoparticles doped with Cr: An experimental and theoretical analysis, *J. Alloys Compd.*, 2020, **849**, 156587.
47 C. Belman-Rodriguez, R. Ponce-Perez, A. M. Reyes, C. A. Galindez-Jamioy, G. Soto, M. H. Farías, J. Guerrero-Sánchez, M. G. Moreno-Armenta, A. Reyes-Serrato and S. A. Aguila, Experimental and theoretical assessment of the Eu^{3+} doped $Bi_4Ge_3O_{12}$, *J. Alloys Compd.*, 2023, **966**, 171567.
48 O. Warschkow, K. Chuasiripattana, M. J. Lyle, B. Delley and C. Stampfl, Cu/ZnO(0001) under oxidating and reducing conditions: A first-principles survey of surface structures, *Phys. Rev. B:Condens. Matter Mater. Phys.*, 2011, **84**, 125311.
49 J. I. Paez-Ornelas, R. Ponce-Perez, H. N. Fernández-Escamilla, E. Murillo Bracamontes, H. A. Borbón-Nuñez, J. P. Corbett, M. G. Moreno Armenta and J. Guerrero-Sánchez, Understanding the Role of Oxygen Vacancies in the Stability of ZnO(0001)-(1 × 3) Surface Reconstructions, *J. Phys. Chem. C*, 2021, **125**, 7980–7989.
50 R. D. Shannon, Revised effective ionic radii and systematic studies of interatomic distances in halides and chalcogenides, *Acta Crystallogr.*, 1976, **A32**, 751–767.
51 S. Brandstetter, P. M. Derlet, S. Van Petegem and H. Van Swygenhoven, Williamson–Hall anisotropy in nanocrystalline metals: X-ray diffraction experiments and atomistic simulations, *Acta Mater.*, 2008, **56**, 165–176.
52 C. Reyes-Damián, R. Álvarez-Chimal, F. Ascencio, J. León-Flores and J. Arenas-Alatorre, Magnetic and optical properties of ZnO nanoparticles and nanorods synthesized by green chemistry, *Nano Exp.*, 2024, **5**, 025006.
53 S. Sharma, C. F. Sánchez Valdés, J. L. Sánchez Llamazares, J. M. Siqueiros and O. Raymond Herrera, Unveiling quantum superparamagnetism by interacting monodomains in multiferroic Er-doped bismuth ferrate nanostructured particles, *J. Phys. Chem. C*, 2021, **125**, 6449–6460.
54 L. Shen, *et al.*, Mechanism of ferromagnetism in nitrogen-doped ZnO: First-principles calculations, *Phys. Rev. B:Condens. Matter Mater. Phys.*, 2008, **78**, 073306.
55 J. Geshev, Interaction plots obtained from in-field magnetization instead of remanence measurements, *J. Magn. Magn. Mater.*, 2018, **467**, 135–138.
56 S. Thamm and J. Hesse, A simple plot indicating interactions, *J. Magn. Magn. Mater.*, 1996, **154**, 254–262.
57 J. Alonso Lopez Medina, *et al.*, Magnetic, structural, and morphological properties behavior of Ni1–xCoxFe2O4 magnetic nanoparticles: Theoretical and experimental study, *Mater. Charact.*, 2024, **216**, 114296.
58 G. Srinet, *et al.*, Structural, optical and magnetic properties of Zn1-xCoxO prepared by the sol–gel route, *Ceram. Int.*, 2013, **39**(6), 6077–6085.
59 M. B. Stearns and Y. Cheng, *J. Appl. Phys.*, 1994, **75**, 6894.
60 R. Wahl, J. V. Lauritsen, F. Besenbacher and G. Kresse, Stabilization mechanism for the polar ZnO(000−1)-O Surface, *Phys. Rev. B: Condens. Matter Mater. Phys.*, 2013, **87**, 085313.
61 J. M. Jacobo-Fernández, C. A. Corona-García, R. Ponce-Pérez, H. A. Borbón-Nuñez, D. M. Hoat, A. Reyes-Serrato and J. Guerrero-Sánchez, Spin-Polarized Total-Energy Calculations on Designing Magnetic Single-Atom Catalysts on the ZnO(000-1) Surface with Pt and Pd, *ACS Appl. Nano Mater.*, 2023, **6**, 16740–16748.